Simulation of pass-by noise of automotive vehicles in the mid-frequency range using Fast Multipole BEM

J. Huijssen [1], **P. Fiala** [1,2], **R. Hallez** [3] **and W. Desmet** [1]
[1] Katholieke Universiteit Leuven, Department of Mechanical Engineering,
Celestijnenlaan 300 B – box 2420, B-3001, Heverlee, Belgium
e-mail: **koos.huijssen@mech.kuleuven.be**

[2] Budapest University of Technology and Economics, Department of Telecommunications,
Magyar tudósok körútja 2., H-1117, Budapest, Hungary

[3] LMS International, Simulation Division,
Interleuvenlaan 68, B-3001, Leuven, Belgium

Abstract
This paper studies the feasibility of acquiring the multiple source-receiver transfer functions for the prediction of pass-by noise Sound Pressure Level (SPL) of vehicles with the Fast Multipole Boundary Element Method (FMBEM). Employing measurements and simulations, the influence of frequency resolution, mesh density, mesh accuracy and solver accuracy on the computation time and on the overall SPL and the third octave band SPL is investigated. It is concluded that pass-by noise estimates with an accuracy of about 4 dB within a computation time of less than one day can be achieved in the near future.

1 Introduction

The maximum sound pressure level (SPL) generated by a vehicle during a pass-by test is an important metric for the vehicle's successful homologation. The ISO 362 standard describes the measurement setup and procedure for obtaining the SPL in several driving modes [1]. As depicted in Fig. 1, the vehicle under test is driving on a specified road surface over at least 20 m along a center line passing between two microphones located left and right at 7.5 m distance and 1.2 m height. The SPL is recorded using a sound level meter with A-weighting and exponential averaging with a 125 ms integration time. Measurements are performed in several pass-by tests with the vehicle driving at a constant speed of 50 km/h and in acceleration, at different gears. The surrounding of the test track is free of large reflecting objects, meteorological conditions are modest and background noise SPL is at least 10 dB below the measured maximum SPL.

As noise restrictions are becoming more and more severe, car manufacturers are in a need to predict the pass-by noise (PBN) sound pressure level of newly developed cars as early in the design stage as possible [2]. Moreover, in order to develop effective countermeasures to reduce the pass-by noise, the various noise sources and their contributions to the overall SPL need to be identified, and there should also be information on the signatures of the sources, either in the form of third octave band SPLs, time-frequency spectra or complete audible sound samples. Recently, several research approaches have been conducted to develop synthesis procedures for the prediction and analysis of pass-by noise [3, 4, 5, 6]. These procedures concern the translation of a number of source excitations in the moving vehicle to the received signals at the microphone positions. Main issues in these procedures are

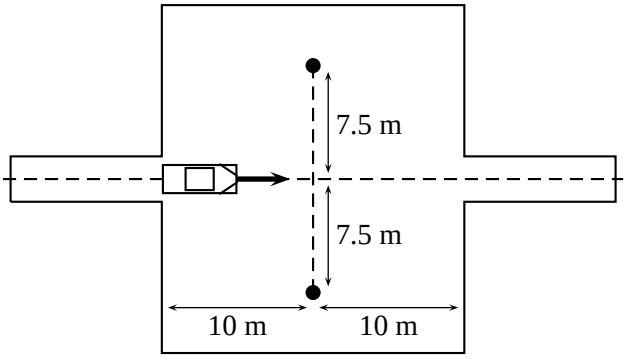

Figure 1: Overview of the setup for a pass-by noise test conform the ISO 362 Standard.

1. The identification and representation of all noise sources.
2. The determination of the source excitations.
3. The acquisition and application of the source-receiver transfer functions for a discrete number of vehicle positions.
4. The application of the Doppler shift due to the movement of the vehicle.
5. The combination of all source contributions into one signal for each receiver.

The first three items involve a considerable amount of experimental effort, and of these the determination of the transfer functions from the sources and vehicle positions to the receivers is considered as the most lavish part [7]. This stems from the large number of source-receiver relationships to be obtained, and from the requirements posed to the measurement environment, being either an outdoor test track or a semi-anechoic chamber that is large enough to contain all significant source-receiver transfer paths.

The employment of computational methods to generate numerical estimates of the source-receiver transfer paths would considerably alleviate the experimental burden of the PBN synthesis procedure. This would also allow vehicle developers to obtain a pass-by noise estimate already during the virtual prototyping stage, as it does not require the availability of a physical prototype for conducting measurements. Another advantage of having such a computational method is the flexibility to study various countermeasures for reducing the PBN sound pressure level. Moreover, we could take our analysis of PBN a level of abstraction up and evaluate various alternative scenarios to the improvement of the ISO 362 Standard, for instance to enhance the standard's representativity for traffic noise annoyance and harm in an urban environment.

Evidently, the required frequency range and resolution are important parameters when applying computational methods for the determination of the source-receiver transfer functions. Depending on the frequency range, various methodologies are available. From the one side, a deterministic approach like the Boundary Element Method (BEM) [8] allows for the accurate prediction of sound fields from arbitrary structures in the low frequency range. The higher frequencies require an increasingly dense surface mesh, and since the computational complexity of the BEM is $\mathcal{O}(N^2)$ to $\mathcal{O}(N^3)$, with N the number of degrees of freedom (DOF), the computational resource demand increases rapidly from considerable to severe. From the other side, asymptotic methods such as Geometric Acoustics and the Geometric Theory of Diffraction [9, 10] are applicable to the high frequency range where the wavelength is much smaller than the geometrical complexity. This type of methods loses its validity for lower frequencies. The mid-frequency range, stretching from about 500 Hz to 2 kHz for the case of the sound field from a complete vehicle, is too high for the conventional BEM and too low for the asymptotic methods.

Recently, new methodologies have been introduced to address the mid-frequency region [11, 12, 13]. The High Frequency Boundary Element Method [14], while being an asymptotic method, seems capable of

yielding satisfactory results for the determination of vehicle exterior sound fields down to frequencies as low as 200 Hz, although results appeared to be less accurate in acoustic shadow regions [15]. Another highly promising candidate is the Fast Multipole Boundary Element Method (FMBEM) [16, 17], which is an approach based on the BEM that exhibits a much more favorable computational complexity of $\mathcal{O}(N \log^2 N)$. Whereas the BEM is usually applied to problem sizes up to several tens of thousands of DOFs, the FMBEM allow the evaluation of problems with sizes up to millions of DOFs in an acceptable computation time. For the computation of acoustic fields of vehicles, Chaigne et al. [18] reported computed predictions of the exterior acoustic panel loads in the range from 400 Hz to 2.5 kHz using the FMBEM. Most results showed less than 5dB deviation as compared to measurements, whereas the panel loads in the shadow regions of the car were underestimated. Cordioli et al. [19] reported results of exterior acoustic loads for a full vehicle in the frequency range from 92 Hz to 1361 Hz using the FMBEM. A similar agreement within 5 dB was found here for the panels close to the source, whereas the larger deviations in the shadow regions were contributed to the lack of geometrical detail in the mesh. The reported computation time of four hours for the entire range (36 frequencies) is promising for realistic situations.

This study investigates the feasibility of employing the Fast Multipole Boundary Element method for the numerical evaluation of source-receiver transfer functions for pass-by noise synthesis. The pass-by noise case requires a broad frequency range, since the various contributing sources contain significant power levels in the low-, mid- and high-frequency ranges. This can be seen from the typical source spectra of exhaust, intake and tire noise shown in Fig. 2. We investigate the ability of the FMBEM to cover the required range with sufficient accuracy and within a reasonable computation time. In this paper the following issues will be addressed separately:

- The frequency resolution
- The density of the mesh
- The accuracy of the mesh geometry
- The accuracy of the FMBEM solver

For each of these issues, accuracy and computation time will be considered. In Section 2 we further discuss the approach to address these issues, including the setup of the conducted measurements and of the simulations. In Section 3 we focus on the frequency resolution and we will pay some attention to the necessity to obtain accurate transfer functions in the spectral domain as well as in the time domain. In the subsequent Sections 4 to 6 the remaining three issues are covered. Sections 7 and 8 close the paper with a discussion of the evaluation time and feasibility of computation, and with the general conclusions.

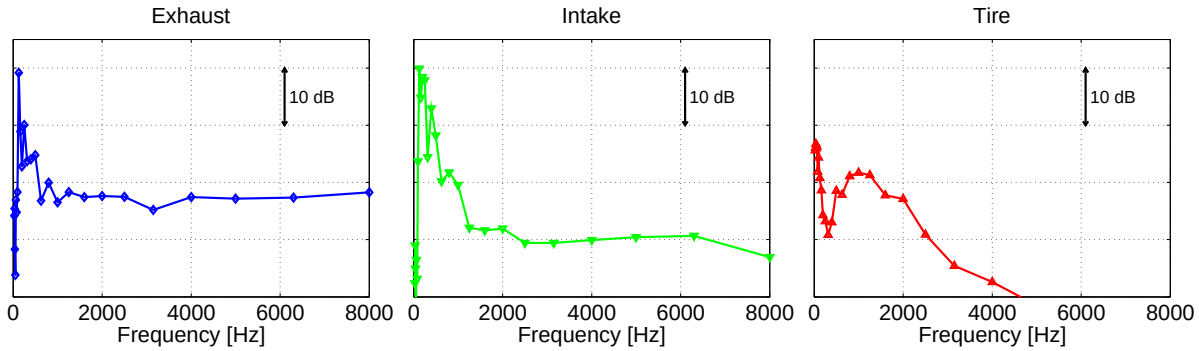

Figure 2: From left to right: typical 1/3 octave band spectra of exhaust, intake and tire noise. All sources exhibit high power levels at frequencies below 1-2kHz and constant or decaying levels at higher frequency bands.

2 Approach

The goal of our simulations is the determination of overall A-weighted SPL and third octave band SPLs at the receiver position, as these parameters are essential for pass-by noise evaluation. The average performance and worst case performance for all of the transfer functions will be discussed in terms of these two metrics. The aim is not to generate synthesized sound samples for sound quality evaluation as in e.g. [4, 5, 6], which would result in considerably stricter requirements for frequency resolution and mesh accuracy than for this study.

In this study we assume that the pass-by noise varies slowly enough and that the effect of Doppler shift is small enough to permit the employment of multiple steady state analyses at different vehicle positions, instead of having to reconstruct the transient signals and use the time-averaged SPL. The steady state SPL that corresponds with the exponentially weighted, time-averaged instantaneous SPL,

$$\mathrm{SPL}(t) = \left[\frac{1}{T}\int_{-\infty}^{t} p^2(\tau)\exp^{(\tau-t)/T}\,\mathrm{d}\tau\right]^{1/2}, \tag{1}$$

T being the decay time of the weighting function, can be obtained from the spectral representation of the pressure $\hat{p}(f)$ as

$$\mathrm{SPL}_{ss} = \left[\frac{2}{T}\int_{f_1}^{f_2} |\hat{p}(f)|^2 \mathrm{d}f\right]^{1/2}, \tag{2}$$

where T is the observation time period and $f_2 > f_1 \geq 0$ are the upper and lower frequencies of the frequency band of interest. For a discrete spectrum $\hat{p}_n$ this integral is evaluated by means of rectangular or trapezoidal integration, where the latter may be employed for increased accuracy in cases where the frequency band is small with respect to the resolution of the spectrum. The multiple steady state approach with SPL_{ss} as metric should suffice for the studies of the transfer functions presented in this paper. However, we do keep in mind that in future analysis the reconstruction of the transient signals will in fact be conducted, and for this reason we require the transfer functions to be represented adequately not only in the frequency domain, as Frequency Response Functions (FRFs), but also in the time domain, as Impulse Response Functions (IRFs).

The focus in this study will be on the determination of the source-receiver transfer functions. For this reason the adequate representation of the sources will not be considered. With regard to the source signatures, the varying source levels over frequency will determine the relative contributions of the different frequency bands. Strong narrowband peaks in the source excitation could result in completely different third octave band levels at the receiver than was expected from the transfer functions alone or from a summation of the third octave band levels of source and transfer function. This will be accounted for in the considerations but it does not significantly change the conclusions of this study. With regard to the geometry of the sources, we assume that the transfer functions can be described as point-to-point source-receiver relations, where each of the sources may be represented as one or more point sources [20]. Other approaches like applying the full normal velocity condition on the sound radiating source surface or using a generic source, as in [21, 22], will be (much) more computationally intensive and are not considered realistic at the moment. Anyhow, an alternative choice in these approaches will not significantly affect the analysis of the transfer functions. Finally, the issue of the coherence of different sources is of importance when accumulating the source contributions into one receiver signal, but this is also disregarded in this paper.

In the study, the source-receiver transfer functions are considered for six source positions, two vehicle positions and one receiver, giving twelve transfer functions in total. As shown in Fig. 3, the source positions 1 to 6 are taken at the rear left tire, exhaust tailpipe and engine intake, and three positions for the direct engine radiation, one below the engine close to the oil pan and two at the front and back of the engine, up in the engine bay. The receiver is on the left of the vehicle, and the selected receiver positions relative to the vehicle position, A and B, are the center and front location as shown in the figure. This set of functions is considered representative for the possible variety of transfer functions that may occur with pass-by noise, and it is therefore expected that the observations and results for this data set are valid for the complete set.

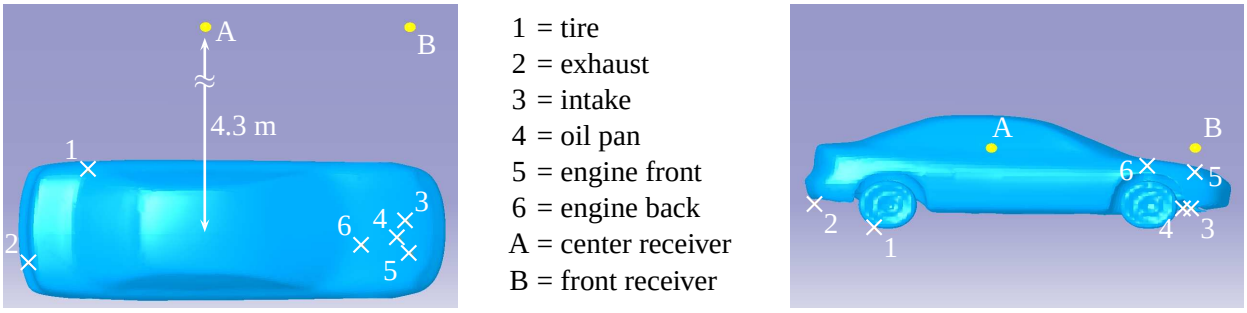

Figure 3: Location of the source and receiver points, top view and side view.

The transfer functions under study have been acquired by measurements as well as by simulations. In the subsequent subsections the experimental and simulation setups are discussed.

2.1 Measurement setup

For the evaluation of the transfer functions, measurements have been conducted on a Chrysler Neon car. The vehicle was positioned in a semi-anechoic room, and the transfer functions were obtained through a reciprocal approach by placing an omnidirectional volume acceleration source in one of the two 'receiver' positions A and B, and by acquiring the sound pressures on the 'source' positions 1 to 6, as in Fig. 3. The positions A and B were set at a lateral distance of 4.3 m to the center line of the car, which was the maximum possible because of the size of the room, and their height was 1 m. These distances are expected to sufficiently represent the distances in the ISO 362 Standard. Due to the semi-anechoic room and the sound source, reliable FRF measurements were expected from 150 Hz and higher. The sampling frequency was 8.2 kHz. Figure 4 shows an overview of the setup and two measured transfer functions.

2.2 Model setup

The simulations were set up to reproduce the experimental configuration. The acoustic surface mesh was derived from the NCAC crash mesh of the Chrysler Neon [23] using mesh editing tools available in the Virtual.Lab CAE software suite [24]. The geometry inside the engine bay consisted of the engine block, the battery and the radiator. Some geometrical details, like the exhaust tailpipe, were missing from the mesh. The mesh was made up from triangular elements with a typical edge length of 50 mm. By subdividing the

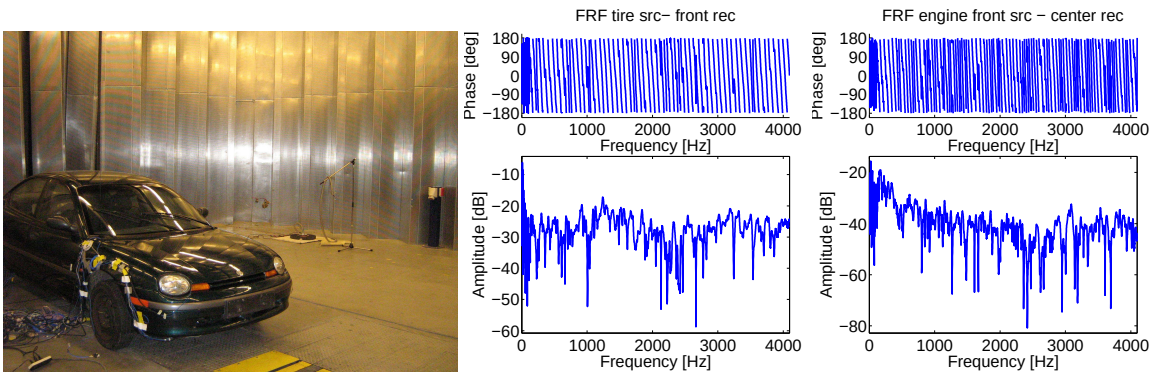

Figure 4: Experimental determination of the transfer functions. Left: overview of the setup. Right: measured FRFs of the tire source - front receiver and engine front source - center receiver positions.

mesh	#nodes	$f_{\max}$	DOFs
L1	15 225	677 Hz	45 631
L2	60 864	1 271 Hz	182 518
L3	243 402	2 446 Hz	730 056

Table 1: Number of nodes and maximum frequency at six points per wavelength of the employed surface meshes, and degrees of freedom (DOFs) for the simulations including the interior impedance boundary condition.

elements, two finer meshes were derived for which some characteristics are listed in Table 1. On the surface of the mesh, a zero velocity boundary condition was assumed, and on the ground plane a symmetry condition was employed. The Fast Multipole BEM solver that was used, as included in the Virtual.Lab suite, is based on the Indirect BEM formulation. Fictitious eigenfrequencies were suppressed by applying an impedance boundary condition on the interior of the mesh, which led to a number DOFs about three times the number of nodes for all three meshes. Because the number of receiver positions was smaller than the number of source positions, a reciprocal approach was used here as well, in which at the 'receiver' positions volume acceleration point sources were defined, and at the 'source' positions clusters of field points were defined where the acoustic pressures were obtained. The clusters of points allow for the assessment of the sensitivity to the exact field point positions. Computations were performed on a Linux cluster employing one or more Intel Xeon processors running at 2.66 GHz, with 4 Gb memory per processor and sufficient scratch disk space available.

3 Frequency resolution

First subject of study is the required frequency resolution for obtaining a reliable estimate of the overall PBN SPL and third octave band SPLs. With the purpose of predicting spatially and frequency averaged third octave band levels on SEA panels, Müller et al. [25] obtained a sufficient resolution of three frequencies per third octave band, and [15] reported a good agreement for spatially and frequency averaged values with an approach taking single frequency samples over a large number of points and an alternative approach taking multiple frequency samples over a limited number of points. Other authors [18, 22] report results at a single frequency. In our case, the interest is not in spatially averaged values, but in single point-to-point relations in terms of frequency-averaged band levels. The number of required frequencies for a sufficiently accurate third octave band average depends on the smoothness of the FRF in that frequency band, which is related to the location of the source and receiver and their direct environment. For instance, the FRFs of the sources inside the engine bay are influenced by its resonant behavior and are likely to contain strong peaks and dips, as can also be seen from the rightmost FRF in Fig. 4.

In order to study the required frequency resolution of the transfer functions, the measured transfer functions were employed as the starting point since they were obtained up to 4.1 kHz and with a fine frequency resolution of 1 Hz. However, as the measurements were inaccurate below about 150 Hz, the measured data was appended with simulated transfer functions in the low frequency range. The simulated results were obtained with a conventional BEM computation on a 6000 node mesh of quadrilateral elements. The mesh allowed for a maximum frequency of 300 Hz at six points per wavelength, and it was derived from the $L1$ mesh in Table 1 by using a mesh coarsener. Measured and simulated data were combined by a gradual transition between 150 Hz and 250 Hz to yield a single FRF for each source-receiver transfer function. Figure 5 shows simulated and measured FRFs for two transfer functions, together with the impulse responses and the correction to the impulse responses by employing the simulated data. In the range 200 Hz –300 Hz the measured and simulated FRFs agree within ± 10 dB, for which Fig. 5 shows a best case and a worst case agreement. The FRFs show a considerable improvement in the low-frequency range, as can best be seen from the phase. However, as can be observed from the impulse responses and their corrections it is not evident that the low-frequency simulated data yield improved impulse responses for these cases, although it

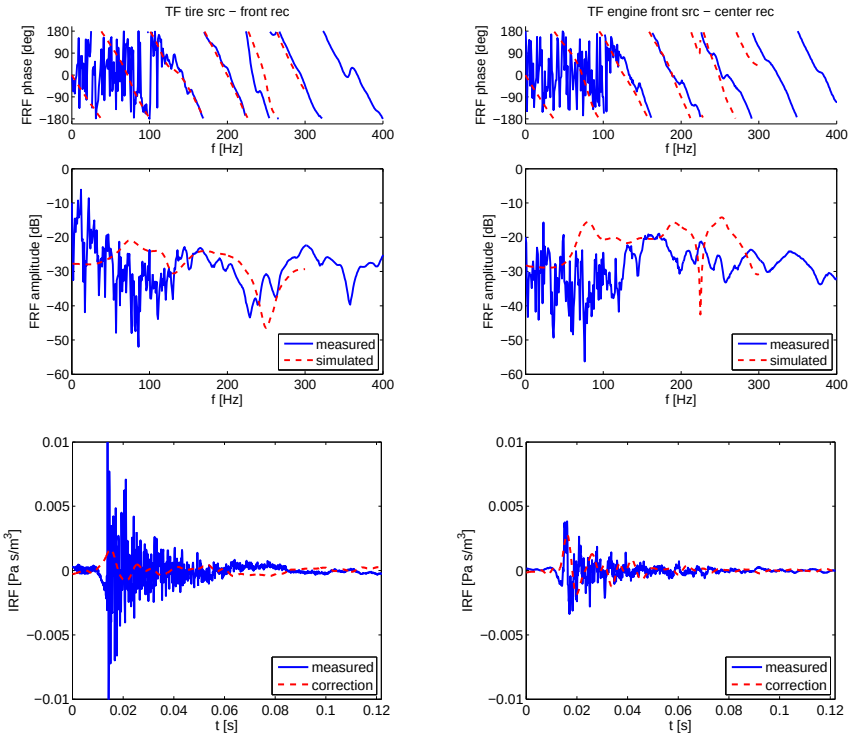

Figure 5: Reconstruction of the low-frequency content of the reference FRFs, shown for the tire source - front receiver (left) and the engine front source - center receiver transfer functions (right). Above: measured and simulated FRFs, phase and amplitude. Below: Measured impulse responses and corrections, i.e. original IRF minus corrected IRF, by replacing the low-frequency content by simulated data.

was clearly observed that for the long times $t = 0.1 \ldots 1.0$ s the impulse responses were improved due to suppression of the low-frequency noise in the measured data.

With these constructed FRFs as reference, the resulting overall SPL[1] and third octave band SPLs are compared to those of FRFs that are subsampled with a frequency step $\Delta f > 1$ Hz. Figure 6 shows estimates of the overall SPL for the six FRFs related to the center receiver versus Δf. It is observed that the deviation with respect to the $\Delta f = 1$ Hz case does not increase monotonously with increasing Δf, and that it varies between the different FRFs. If all mean and maximum deviations of the twelve FRFs are combined in one figure, as in Fig. 7, left, then it becomes clear that for a maximum deviation of 1 dB in the overall SPL Δf may go up to 50 Hz over the entire frequency range. Figures 7, middle and right, show the mean and maximum deviations of the third octave band SPLs versus Δf for all FRFs combined. It is observed that the higher frequency bands allow for a coarser sampling than the lower frequency bands, which is likely related to the larger width of the higher bands. Table 2 summarizes the allowable Δf for a maximum deviation of about ± 1.5 dB. In the light of these findings, the required frequency resolution needed for point-to-point relations is considerably higher than the three frequencies per third octave band as was found by Müller et al. for spatially averaged panel loads [25]. This can also be seen by comparing the blue, continuous and green, dashed lines in the figures. Moreover, employing only the single center frequency as an estimate of the third octave band SPL can hardly lead to reliable results, as can be seen from the red, dash-dotted line in the figures.

[1]That is, the SPL in the receiver points as obtained by multiplying the FRFs with a constant source level.

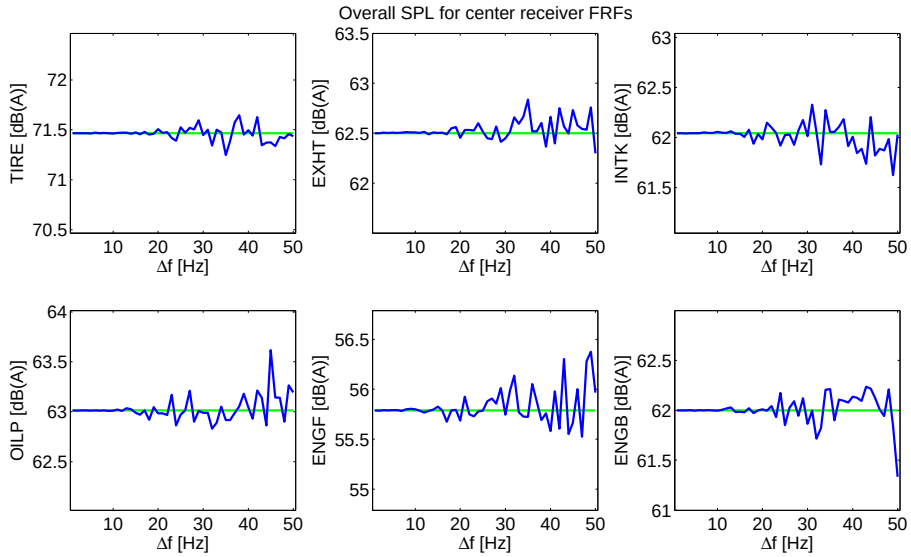

Figure 6: Estimates of the overall SPL for the six FRFs related to the center receiver versus frequency step.

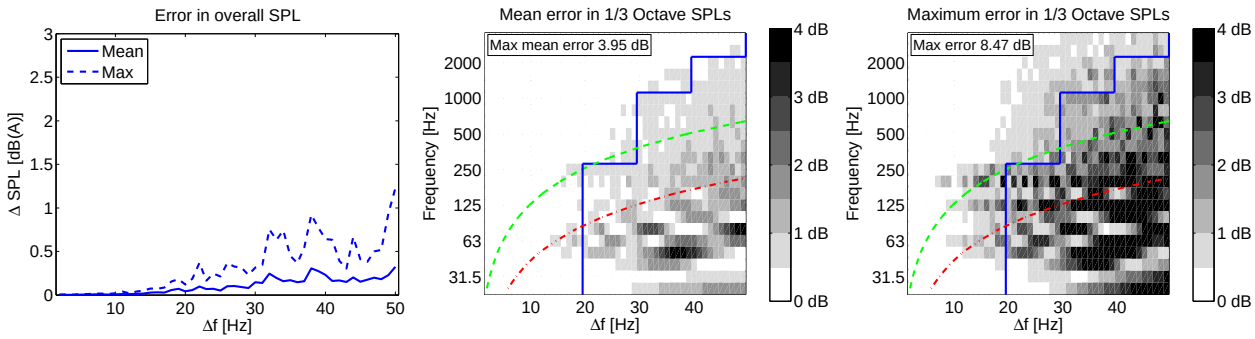

Figure 7: Relative errors for all twelve FRFs versus increasing frequency step. Left: mean and maximum error over all FRFs for the overall SPL. Middle and right: mean and maximum error over all FRFs in the third octave band SPLs. The color axis in the middle and right figures is limited to 4 dB. The blue, continuous line demarcates the maximum Δf for a mean error in the 1/3 octave band SPLs less than 0.5 dB and a maximum error less than 1.5 dB. The green, dashed line and the red, dash-dotted line show the frequency step related to the rules prescribing three frequencies and one frequency per third octave band.

frequency range	Δf
$<$ 282 Hz	20
282 Hz . . . 1.1 kHz	30
1.1 kHz . . . 2.2 kHz	40
$>$ 2.2 kHz	50

Table 2: Maximum frequency step in different frequency ranges for obtaining a deviation less than ± 1.5 dB in the third octave band SPLs and of ± 1 dB in the overall SPL.

3.1 FRF interpolation

Although we have confined our attention in this paper to steady-state analyses and frequency domain considerations, in the context of the pass-by noise case we require the transfer functions to be represented adequately not only in the frequency domain as FRFs, but also in the time domain as IRFs. However, since the time period T of the impulse response function is inversely proportional to the frequency step Δf, for a coarse frequency resolution the time period becomes too small to contain the entire impulse response. This would result in time-domain aliasing which should be prevented. For instance, for the IRFs in Fig. 5 the pulse duration is about 0.1 s, and this would allow for a maximum of $\Delta f = 10$ Hz. If a coarser frequency resolution is employed for the simulation of the FRFs, then the intermediate FRF values may be acquired by interpolation to yield a sufficiently high frequency resolution. The need for an identical frequency step over the entire axis for the time-domain reconstruction is another motivation for FRF interpolation if we want to apply the variable frequency resolution as suggested in Table 2. A third important reason for FRF interpolation is that the source spectrum may require a finer frequency resolution than the transfer functions because of its irregular pattern, for instance in case of strong harmonic content due to engine orders or otherwise. In this case the relative smoothness of the transfer function would allow for an FRF interpolation scheme to yield satisfactory results using a coarser resolution without the need for expensive computations on all intermediate frequencies.

The interpolation of the FRF can be performed by local function approximation using real functions either for the real and imaginary parts or for the magnitude and phase parts of the FRF. Fig. 8 shows the maximum error in the SPL versus frequency step for the real/imaginary and the magnitude/phase approaches using interpolation with cubic splines.

As compared to subsampling, the magnitude/phase interpolation does not significantly affect the results, whereas the real/imaginary interpolation yields a considerable deterioration. Generally, the magnitude and phase[2] are much smoother functions than the real and imaginary parts. Moreover, as the SPL metric is based on the magnitude of the spectrum, see Eq. (2), the magnitude/phase interpolation fits better to the prediction of SPL. Besides these two approaches, an alternative approach employing complex rational functions [26] has been investigated but it only yielded satisfactory results for frequency resolutions $\Delta f < 20$ Hz. In conclusion, the magnitude/phase interpolation with cubic splines is the preferred approach of FRF interpolation.

Instead of comparing the third octave band SPLs and overall SPL of the subsampled FRFs as in Fig. 7 we may now compare the interpolated FRFs with the reference FRFs frequency-per-frequency. Figure 9 shows the mean and maximum of all single frequency error for the SPL in the dB scale for the third octave bands and for the entire range. Compared to Fig. 6 these figures result in a much more conservative estimate of

[2]This holds only for the non-periodic phase, as the periodic phase exhibits sharp transitions over the $[-\pi, \pi)$ boundaries.

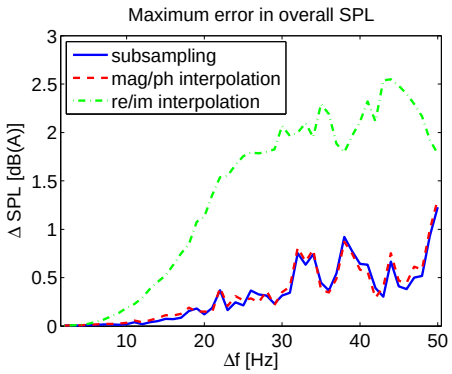

Figure 8: Maximum errors in overall SPL for all twelve FRFs versus frequency step, for the magnitude/phase and real/imaginary interpolation of the FRF.

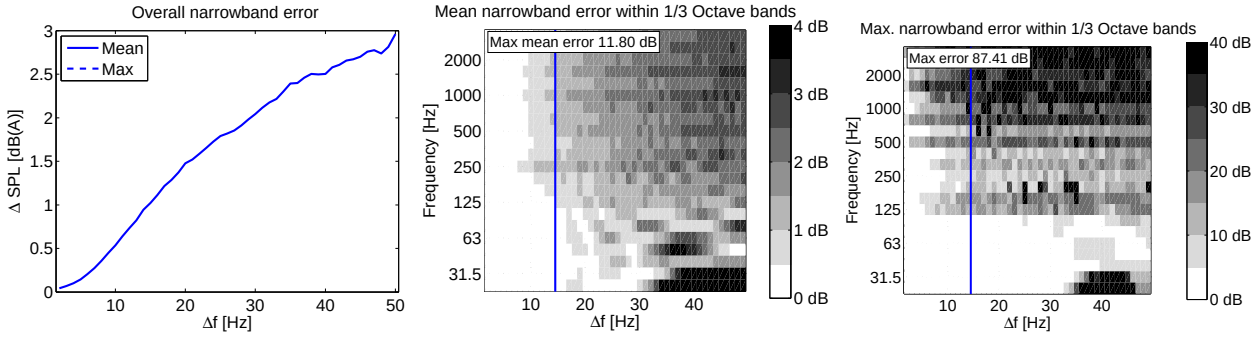

Figure 9: Relative frequency-per-frequency errors for all twelve FRFs versus increasing frequency step. Left: mean and maximum error over all FRFs for the complete frequency range. The maximum error line falls beyond the limit of the axis. Middle and right: mean and maximum error over all FRFs in the third octave bands. The color axis in the middle figure is limited to 4 dB and in the right figure to 40 dB. The line demarcates the maximum Δf for a mean error in the 1/3 octave bands less than 1 dB. However, up to this line the *maximum* error can go up to 35 dB.

the frequency step of $\Delta f = 15$ Hz over the entire frequency range to obtain the same accuracy for the *mean* deviations as for the *maximum* deviations in Table 2. The maximum errors are generally in the order of 10-80 dB, which makes clear that the interpolation may lead to large errors for single frequencies, especially for the higher frequency steps. The sudden jump in the third octave SPLs around the 125 Hz band is caused by the reference FRFs consisting of simulated data up to 150 Hz and measured data beyond. The simulated data are smoother than the measured data and therefore give rise to less interpolation error. The interpretation of the two different requirements for the frequency step is that the estimate of Table 2 holds in case of source excitations with a smooth, broadband characteristic, while the $\Delta f = 15$ Hz estimate is more representative in case of excitations with strong tonal components. These may lift up errors at single frequencies and thus influence the overall and third octave band SPL disproportionally.

4 Mesh density

Since the mesh density determines the mesh size and consequently the complexity of the BEM model, this is an essential parameter for the feasibility of obtaining simulated transfer functions for pass-by noise prediction. The common rule of thumb for the mesh density is to use six to ten elements per wavelength to obtain an error of about 1.0 - 1.5 dB in the acoustic field point pressures [27]. For spatially and frequency averaged SPL values, Müller et al. [25] concluded that six elements per wavelength resulted in an error of 4 dB, which was considered acceptable, whereas a 4.5 elements per wavelength mesh resulted in an unacceptable error of 10 dB. Wang et al. [15] however reported results for simulations with a conventional BEM which showed agreement with measurements within 5 dB up to a resolution in the order of two elements per wavelength. And even more surprising, Zhang et al. [22] reported good agreement within 1 dB of PBN SPL between measurements and simulation results employing an Indirect BEM approach for frequencies up to 3 kHz whereas the density of their mesh seemed to allow for a maximum frequency of no more than 300 Hz at six elements per wavelength. These results show that, even though the rule of thumb of six elements per wavelength is well established for single frequency results, there is some disagreement in the literature when spatially/frequency averaged values are concerned. In addition to this, a somewhat relaxed rule of thumb that is encountered in the industrial context is to ensure that only 80% of the elements obey the six elements per wavelength rule.

The required mesh density is studied on the basis of the $L1$ surface mesh of the Chrysler Neon and the refined $L2$ and $L3$ meshes as given in Table 1. Results on coarser meshes are compared to those on finer meshes. On

the $L1$ mesh, all FRFs were obtained over the range from 1 Hz up to 2240 Hz using the steps given in Table 2. A conventional indirect BEM was employed up to 660 Hz and the Fast Multipole BEM was employed from 160 Hz onwards. The numerical integration of the BEM solver, as provided by Virtual.Lab, employed a level 2 quadrature rule in all regions. The residual error of the iterative solver in the FMBEM was set at 10^{-3}. Figure 10, left, shows the mean and maximum deviations of the FMBEM with respect to the BEM for all FRFs over the overlapping frequency range. The average deviation over the frequency range is 0.4 dB, which is in line with the expected accuracy of the FMBEM. However, for some FRFs and at specific frequencies the deviation may go up to 4-8 dB. On the $L2$ mesh, all FRFs were obtained over the range from 400 Hz up to 2240 Hz employing the FMBEM. On the $L3$ mesh, the FRFs were obtained only on the frequencies $[1200, 1240, 1680, 1720]$ Hz because of the considerable computational load. Figure 10, right, presents the mean and maximum deviations for the FRFs obtained with FMBEM on the $L1$ mesh compared to those obtained on the $L2$ mesh over the range 400 Hz – 1200 Hz. The mean deviation is steadily increasing, but from 900 Hz the maximum deviation becomes irregular. This shows that for coarser meshes beyond the six elements per wavelength rule the estimation at single frequencies and for point-to-point relations becomes more and more unreliable. Table 3 summarizes mean and maximum deviations of the $L1$ and $L2$ meshes at four different frequencies. At the frequencies 880 Hz and 1720 Hz, the $L1$ and $L2$ meshes respectively obey the six points per wavelength rule for 80% of their elements. These data show that, in order to keep the maximum error at a single frequency below 2 dB, the six elements per wavelength rule must be respected. However, it is also clear that the error does not increase dramatically for coarser meshes, and that taking six elements per wavelength for only 80% of the elements can yield an acceptable accuracy as well, not only for frequency averaged quantities but even when looking at single frequency results.

When looking at the third octave band SPL and overall SPL, the situation seems even more relaxed. Figure 11 displays the overall SPL for all FRFs obtained with the $L1$ mesh for 1 Hz – 2240 Hz and obtained with the $L2$ mesh for 400 Hz – 2240 Hz, where the frequencies below 400 Hz are taken from the $L1$ mesh results. Although the $L1$ and $L2$ meshes are clearly too coarse for this frequency range, with 1.8 and 3.4 elements per wavelength at 2240 Hz respectively, the agreement in the SPL within 0.5 dB for all FRFs is remarkable. Figure 12 shows a best case and worst case agreement of the third octave band SPLs of two FRFs, showing a maximum deviation of 3 dB in the 2 kHz third octave band.

These results demonstrate that for a sufficiently accurate prediction of overall and third octave band SPL for pass-by noise the six elements per wavelength is not necessarily the limit. From Figure 10 and Table 3 it appears that the mean deviations over all FRFs remain below 1 dB down to three to four elements per wavelength, although the maximum deviations become considerable. Although the frequency averaged results in the form of overall and third octave band results seem to suggest that we can even go down to two elements per wavelength, we have to bear in mind that, with the incorporation of the source excitations in the pass-by

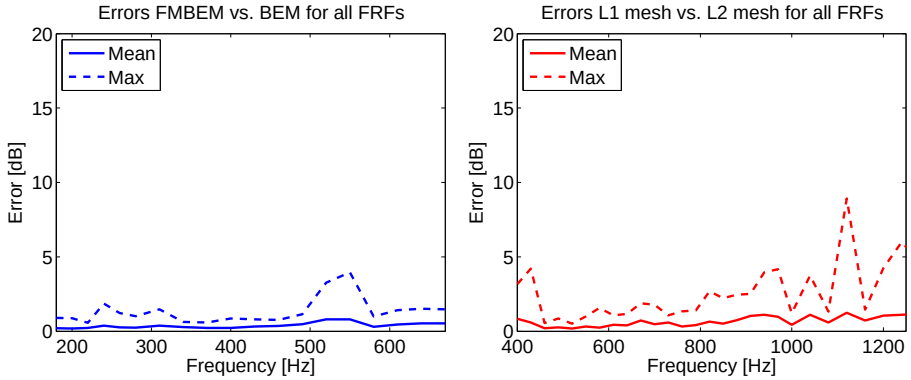

Figure 10: Left: Mean and maximum error for all FRFs obtained with FMBEM compared to BEM on the $L1$ mesh. Right: Mean and maximum error for all FRFs obtained with FMBEM on the $L1$ mesh compared to the $L2$ mesh.

Frequency [Hz]	Ref. mesh	$L1$ mesh Elements per λ	$L1$ mesh Deviation [dB] mean	$L1$ mesh Deviation [dB] max	$L2$ mesh Elements per λ	$L2$ mesh Deviation [dB] mean	$L2$ mesh Deviation [dB] max	$L3$ mesh Elements per λ
670	$L2$	**6.1**	**0.7**	**1.9**	11			
880	$L2$	**4.6**	**0.8**	**2.5**	8.7			
1240	$L3$	**3.3**	**1.1**	**3.6**	**6.2**	**0.5**	**2.4**	12
1720	$L3$	2.4	2.6	10.3	**4.4**	**0.7**	**3.6**	8.5
2240	$L3$	1.8	4.7	11.9	**3.4**	**0.7**	**2.0**	6.5

Table 3: Mean and maximum deviations for all FRFs obtained on a number of frequencies employing the $L1$ and $L2$ meshes, as compared to results obtained on a finer reference mesh.

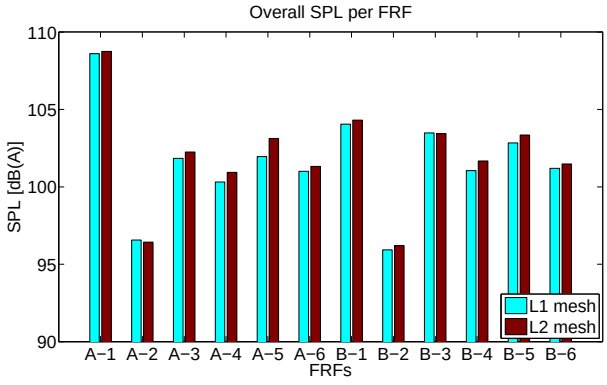

Figure 11: SPL obtained with FMBEM simulations on the $L1$ mesh and the $L2$ mesh up to 2240 Hz.

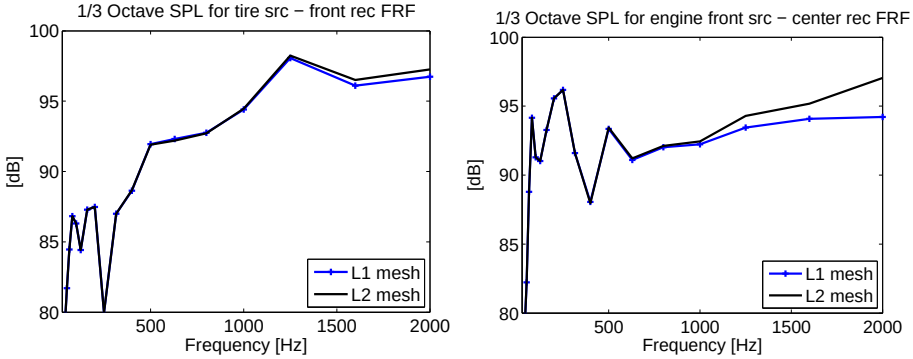

Figure 12: Third octave band SPLs for two FRFs, showing the best case and the worst case agreement between the simulations on the $L1$ and $L2$ meshes.

noise estimates, the image of averaged values may be considerably distorted because of lifting out certain frequencies and thus magnifying the errors in the transfer function at those frequencies. For this reason it is suggested not to go any lower than 3.5–4.5 elements per wavelength, the latter of which in our case came down to having 80% of all elements satisfying the six elements per wavelength criterion.

5 Mesh accuracy

In order to reproduce the measured transfer functions by means of simulation, it is essential that the model adequately represents the physical configuration. Important aspects here are the geometry of the mesh, the material description of the surfaces and the locations and geometries of sources and receivers. With regard to the mesh geometry, the level of exactness up to which mesh and structure should agree is determined by the wavelength of the acoustic field. However, if the locations of sources and/or receivers lie close to the structure or inside a cavity, e.g. the engine bay, geometrical detail, even of dimensions below the wavelength, may significantly influence the acoustic field. Other small details further away from source and receiver can often safely be disregarded.

Müller et al. [25] showed that a model with only overall geometrical information may yield spatially and frequency averaged values with a deviation of up to 3 dB. Our case concerns the point-to-point relations of sources from various positions close to the mesh to receivers far away from the mesh. The influence of mesh accuracy is studied by starting with the 50 mm surface mesh of the Chrysler Neon and re-meshing it with the Wrapper functionality in Virtual.Lab with two larger element sizes of 80 mm and 160 mm. This approach yields approximate meshes to the 50 mm reference mesh. Subsequent subdivision of the elements results in meshes that have a similar mesh density as the $L1$ and $L2$ versions of the reference mesh, but that also include a coarser $L0$ level mesh with a maximum frequency of about 300 Hz at six elements per wavelength. With each mesh, the FRFs are obtained with the FMBEM for the range 1–2240 Hz using the frequency resolution of Table 2. The $L0$, $L1$ and $L2$ meshes are employed up to 340 Hz, 670 Hz and 2240 Hz respectively, where at the latter frequency the mesh fits about 3.5 element per wavelength. Figure 13 shows mean and maximum deviation for all FRFs of the 50 mm mesh as compared to the measurements (left), and of the 80 mm and 160 mm mesh as compared to the FRFs obtained with the 50 mm mesh (middle and right). From the leftmost graph it may be observed that the frequency-per-frequency agreement between the 50 mm reference mesh and the measurements is not good. The mean deviation over all FRFs and frequencies is about 8 dB with maximum deviations going up to 40 dB. This deviation is larger than the mesh-to-mesh deviation of the two right graphs. Mean deviations go up to 6 dB for the 80 mm mesh and 8 dB for the 160 mm mesh. The latter shows considerable deviation already at lower frequencies. These graphs demonstrate that the influence of mesh accuracy is related to the frequency of the acoustic field. If expressed in overall SPL or third octave band averages, as in Figs. 14 and 15, the deviations between the three meshes is about 2 dB, where the 80 mm

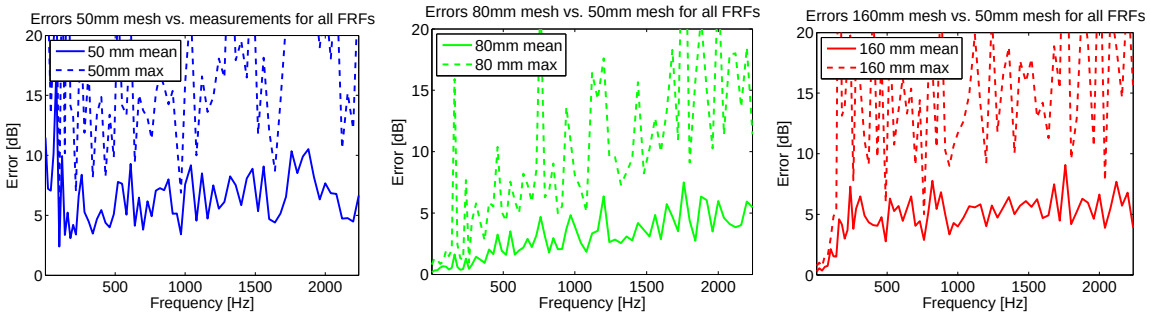

Figure 13: Mean and maximum error for all FRFs. Left: simulations on the 50 mm mesh compared to the measurements. Middle and right: simulations on the 80 mm and 160 mm meshes compared to simulations on the 50 mm mesh.

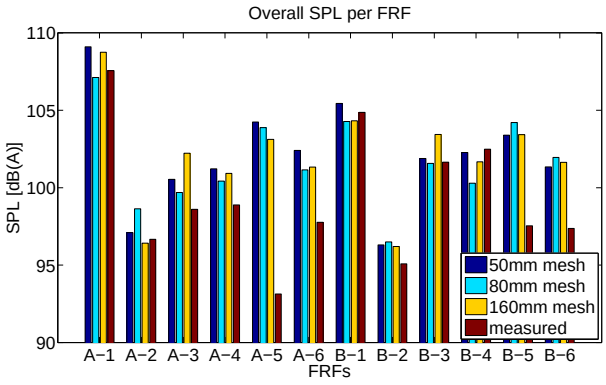

Figure 14: SPL obtained with simulations on the various meshes and with measurements, all up to 2240 Hz.

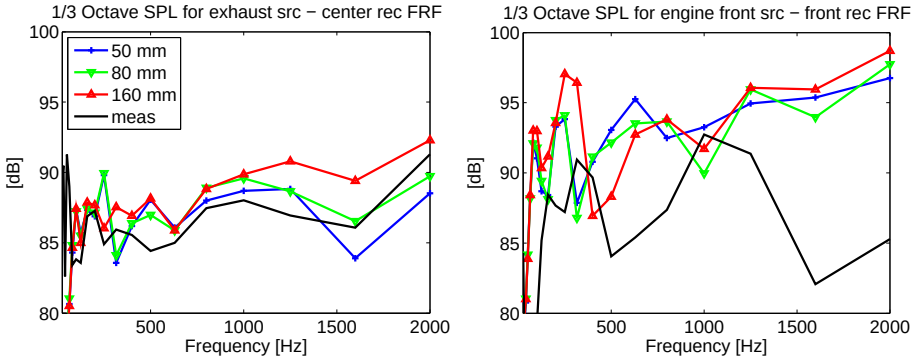

Figure 15: Third octave band SPLs for two FRFs, showing the best case and the worst case agreement between the simulations on the various meshes and the measurements.

mesh and 160 mm mesh perform more or less similar. As compared to the measurements, clearly the FRFs inside the engine bay, numbers 5 and 6 in Fig. 14, are represented worst, whereas FRFs of source-receiver relationships with a less complicated transfer path agree within 3 dB with all mesh results.

The deviation of the FRFs of interior engine bay sources can be explained by an inadequate representation of the configuration. This can be attributed to errors in the locations of the sources, incorrect geometry, incorrect surface description and a vibro-acoustically decoupled evaluation. With regard to the locations of the sources, there was no strong influence found for any of the sources when the location of each source point (i.e. receiver point in the reciprocal simulations) was changed by ± 5 cm in all possible directions. However, with regard to the mesh geometry, the physical geometry in the engine bay is poorly represented by the mesh, as it includes only the engine block, the battery and the radiator. An improvement here should likely lead to improved results of the FRFs. Moreover, if the engine bay content would be represented more thoroughly, then their surface impedances should probably also be taken into account. Although Müller et al. [25] observed no considerable improvement when using realistic impedances on the mesh as compared to using a rigid boundary condition, they did not consider the engine bay content. Moreover, especially in the engine bay, under the hood, the structure may vibrate along with the acoustic excitation and it would require a coupled vibro-acoustic model evaluation to resolve this. Most likely, the main factor in the deviations between computations and measurements is the structural geometry. With the availability of more accurate CAD models, it should be able to improve the prediction of the transfer functions.

6 Accuracy of the FMBEM solver

The FMBEM solver is based on an iterative solver for the system matrix equation. For an iterative solver, the residual error is the stopping criterion that decides whether the obtained solution is sufficiently accurate. A rule of thumb for obtaining sufficient accuracy is to use a residual error of $\rho = 0.001$. For large problems this may however yield an increasing number of iterations to be performed, and it would be beneficial to iterate just up to the required level of accuracy in the results instead of gaining an unnecessary accurate answer for a considerable amount of computation time.

The current investigation concerns the effect to the field results of raising the residual error from $\rho = 0.001$ to $\rho = 0.01$. The FRFs have again been obtained with the 50 mm mesh within the frequency range 1 Hz – 2240 Hz. Figure 16 shows the mean and maximum error for all FRFs over the frequency range. The mean error is about 2 dB over the entire range, and the maximum error may go up to 16 dB for specific frequencies and FRFs. The overall SPL per FRF is shown in Fig. 17, and third octave band plots of two FRFs are shown in Fig. 18. These graphs show the same 2 dB deviation which however depends strongly on the specific source-receiver relationship. This error is in the same range as other errors described in this paper. It depends on the effective gain in time by increasing the residual error whether this remedy is worth applying. This will be discussed in the subsequent section.

7 Evaluation time

Figure 19, left, shows evaluation times per frequency for the three meshes employing four processors on the Linux cluster. All three meshes first have a decrease in the evaluation time and then again an increase (for the $L3$ mesh, this effect would probably come at higher frequencies). The first decrease comes from the improving efficiency of the FMBEM since with higher frequencies the near field is smaller. In FMBEM, the evaluation of near field interactions requires the setting up and evaluation of a conventional BEM matrix, which is entirely stored on the scratch disk. This results in a considerable amount of disk access time which slows down the evaluation. Figure 19, right, shows the disk space needed for evaluation, which exhibits the same trend in the lower frequencies. In the higher frequencies, the slight increase in evaluation time is caused by the increasing size of the cluster tree. On average, the evaluation of a single frequency takes 0.4 hour for the simulations employing $L1$ mesh and 1.4 hour when employing the $L2$ mesh, both on four processors. This factor four time increase clearly shows the nearly linear time dependency of the FMBEM on the number of DOFs. For computations on the $L3$ mesh, evaluation time is largely overshadowed by disk communication due to the large data files at the lower frequencies, but for frequencies in the range 1700–

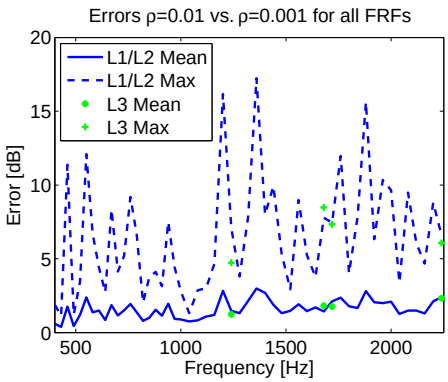

Figure 16: Mean and maximum error for all FRFs of simulations with $\rho = 0.01$ residual error compared to simulations with $\rho = 0.001$.

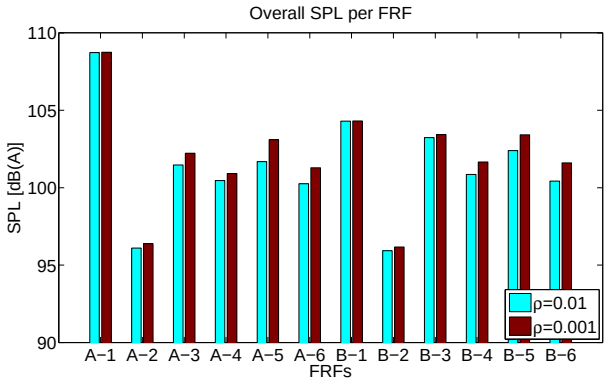

Figure 17: SPL obtained with simulations with $\rho = 0.01$ and $\rho = 0.001$ residual errors up to 2240 Hz.

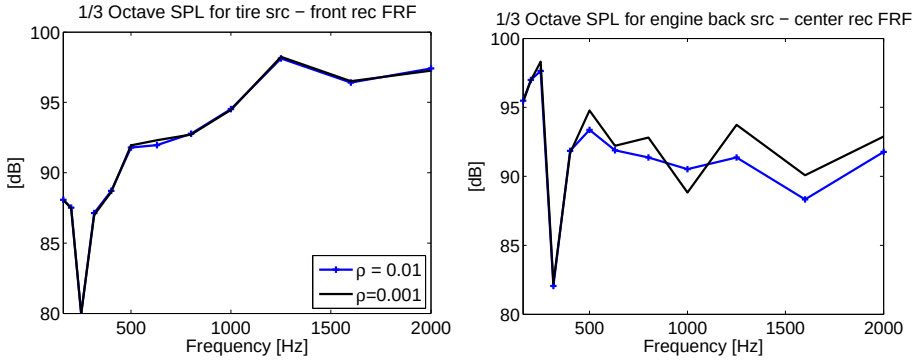

Figure 18: Third octave band SPLs for two FRFs, showing the best case and the worst case agreement between the simulations with $\rho = 0.01$ and $\rho = 0.001$ residual errors.

2000 Hz an evaluation time of 6 hours per frequency is attained, which also confirms the nearly linear time dependency of the FMBEM.

The gain in evaluation time by increasing the residual error of the iterative solver in the FMBEM is shown in Fig. 20, left. For both the $L1$ and $L2$ meshes, the speedup is about a factor 1.4. As was discussed in Section 6, this speedup comes at a cost of accuracy of on average 2 dB and at maximum 16 dB for our problem.

Figure 20, right, shows the speedup realized by increasing the number of processors, which shows that a speedup of a factor 4–5 is attained when evaluating on eight processors instead of on one. When going from four to eight processors, the speedup is about a factor 1.5–1.6. The larger $L2$ mesh evaluation results in a higher speedup, which shows that in that case the overhead cost plays a smaller role than with the smaller $L1$ mesh. This indicates that evaluations with even larger meshes will benefit more from increased parallel evaluation.

To estimate the feasibility of obtaining the transfer functions for predicting pass-by noise SPL with the FMBEM, we consider a typical case in which we require six point sources for the engine, i.e. one for each side, and point sources for intake, exhaust and each of the tires, giving 12 sources in total. Conform Table 2, going up to the 2 kHz third octave band requires the evaluation of 70 frequencies. Employing the meshes up to a frequency for which 80% of the elements satisfies the six elements per wavelength criterion, and a residual error of the iterative solver of $\rho = 10^{-3}$ the total wall clock evaluation time on eight processors for obtaining all surface potentials would then be about 460 hours and with the errors in all approximate steps added together would yield a mean error over all FRFs of about 1.5 dB. The postprocessing step that yields the transfer functions to the receivers relative to all vehicle positions yields only a small added

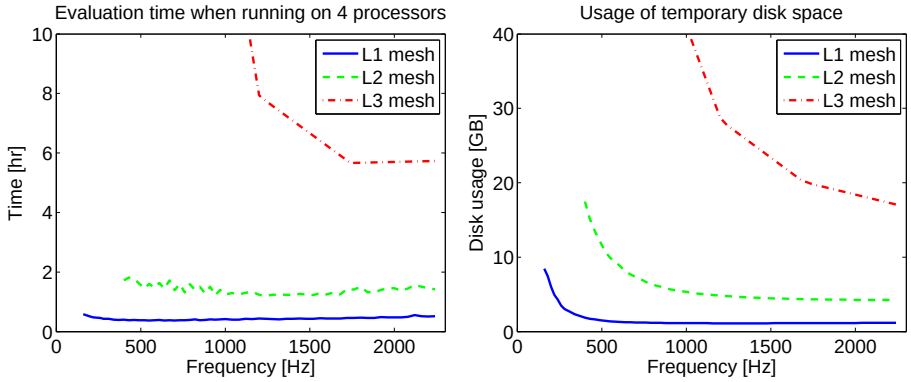

Figure 19: Left: evaluation time per frequency for the $L1$, $L2$ and $L3$ meshes, respectively employing 45k, 183k and 730k DOFs and running on four processors. Right: employed temporary disk space for the three meshes.

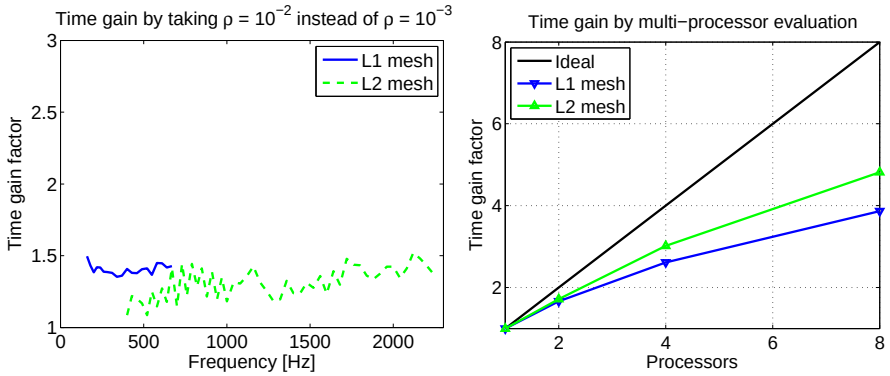

Figure 20: Left: evaluation time gain when increasing the residual error from $\rho = 10^{-3}$ to $\rho = 10^{-2}$. Right: evaluation time gain when employing more processors.

computational effort and is not regarded in this estimate. Lowering the mesh density criterion to 3.0–3.5 elements per wavelength results in 200 wall clock hours and a mean error of about 2.0 dB, and if on top of this the residual error is increased to $\rho = 10^{-2}$, a total wall clock time of 150 hours is obtained with a mean error of 4.0 dB. This is an acceptable error for our purposes.

Although this is still a considerable amount of computation time, further reduction may be achieved by a number of remedies. Firstly, increased parallel evaluation straightforwardly reduces the wall clock time by simultaneous evaluation of different sources or frequencies, provided that not only the number of processors is increased but also the number of hard disks that are addressed independently. Secondly, the measure to suppress fictitious eigenfrequencies may be considerably relaxed by applying an impedance boundary condition on only 10–20% of the interior of the mesh instead of on the whole mesh [28]. This will reduce the number of DOFs by more than a factor two with a consequent equal reduction in computation time. Thirdly, the application of a Singular Value Decomposition (SVD) may reduce the number of right hand sides in the system equation that are derived from the 12 sources [29]. Fourthly, the realization of a broadband implementation of the FMBEM can also result in an improvement of the evaluation time [30, 31]. Of these remedies, the first three may be readily incorporated in the procedure and they will easily lead to a reduction of the wall clock computation time to less than a day. This shows that the numerical evaluation of the transfer functions for the estimation of pass-by noise overall SPL and third octave band SPL is becoming feasible in the near future.

8 Conclusions

This paper has discussed the feasibility of acquiring source-receiver transfer functions for the prediction of pass-by noise overall SPL and third octave band SPLs by means of the FMBEM. It became clear that with an accuracy of about 4 dB this is indeed feasible, although a further reduction of the computation time is still required. This reduction can readily be attained in the near future. In the paper, thorough analyses were performed with regard to the required frequency resolution, mesh density, mesh accuracy and accuracy of the FMBEM solver, and the consequences for the resulting error in overall and third octave band SPL and computation times have been discussed on the basis of twelve source-receiver FRFs which have been measured and computed. For the frequency step it is concluded that, depending on the frequency, a frequency step between 20 Hz and 50 Hz is required for sufficient accuracy. The mesh density is seen to be sufficient when 80% of the elements satisfy the criterion of six elements per wavelength, and a further reduced criterion of to 3–3.5 elements per wavelength for all elements is seen to not excessively increasing the mean error. With regard to the mesh accuracy, comparison between measurements and simulations showed an agreement within 8 dB over the entire frequency range, and it is seen that the accuracy of the mesh considerably influences the accuracy of the transfer functions, especially for mesh parts close to source positions. The sources inside the engine bay where observed to be the most affected by the mesh accuracy. With regard to the accuracy of the FMBEM solver, it was found that an increase of the residual error by one order would result in a mean error of about 2 dB. Clearly, the aim of obtaining averaged quantities, i.e. the SPL and the third octave band SPL, instead of accurate frequency-per-frequency results has shown to considerably relax the requirements for the mesh density and accuracy and for the solver accuracy. With the FMBEM, these can be beneficial to yield sufficiently accurate answers in reduced computation time.

Currently, the evaluation time for obtaining the required transfer functions for pass-by noise estimation is still considerable. However, a number of approaches has been suggested to significantly reduce the evaluation time, and it is esteemed that within the near future it will become possible to obtain numerical predictions of the pass-by noise SPL with the employment of the Fast Multipole Boundary Element Method with an acceptable accuracy and within a limited wall clock evaluation time.

Acknowledgements

We gratefully acknowledge IWT Vlaanderen for supporting the project IWT-070337 MIDAS next generation numerical tools for mid-frequency acoustics. Furthermore, we kindly acknowledge the European Commission for supporting the Collaborative Project CP-218508 MID-MOD mid-frequency vibro-acoustic modelling tools. Finally, we thank Dirk von Werne (LMS Engineering Services) for conducting and supervising the FRF measurements and Karl Janssens (LMS Test Division) for providing generic source data.

References

[1] ISO IS 362-1:2007, *Measurement of noise emitted by accelerating road vehicles – Engineering method – Part 1: M and N categories*, International Organization for Standardization, Geneva, Switzerland (2007).

[2] H. Vanderauweraer, J. Leuridan, *The new paradigm of testing in today's product development process*, Proc. ISMA2004, Leuven, Belgium (2004), pp. 1151-1170.

[3] E. Bongini, S. Molla, P.E. Gautier, D. Habault, P.O. Mattéi, F. Poisson, *Synthesis of noise of operating vehicles: development within SILENCE of a tool with listening features*, in B. Schulte-Werning et al. (eds), *Noise and Vibration Mitigation for Rail Transportation Systems - Proceedings of the 9th International Workshop on Railway Noise, Munich, Germany, 4 - 8 September 2007*, Munich (2008), pp. 320–326.

[4] K. Genuit, S. Guidati, A. Fiebig, *Simulated pass-by noise using microphone array and noise synthesis technology*, Proc. Aachen Acoustics Colloquium 2009, Aachen, Germany (2009), pp 121–132.

[5] D. Berckmans, *Tools for the synthesis of traffic noise sources*, PhD. thesis, Katholieke Universiteit Leuven, Leuven, Belgium (2010).

[6] D. Berckmans, B. Pluymers, W. Desmet, P. Sas, *Numerical comparison of source quantification techniques and equivalent source models for use in sound synthesis systems*, Acta Ac. with Ac., reply to reviewers submitted (2010).

[7] W. Stücklschwaiger, *Experimental pass-by noise source analysis*, Public report D.D10, European Research Project SILENCE (2006), www.silence-ip.org.

[8] R. D. Ciskowski, C. A. Brebbia (eds.), *Boundary elements in acoustics*, Computational Mechanics Publications and Elsevier Applied Science, Southampton/London (1991).

[9] J. Allen, A. Berkeley, *Image method for efficiently simulating small-room acoustics*, J. Acoust. So. Amer., Vol. 65, No. 4 (1979), pp 943-950.

[10] N. Tsingos, T. Funkhouser, A. Ngan, I. Carlbom, *Geometrical theory of diffraction for modeling acoustics in virtual environments*, SIGGRAPH 2000 Conference, New Orleans (2000).

[11] I. Harari, *A survey of finite element methods for time-harmonic acoustics*, Comp. Methods in Appl. Mech. and Eng., Vol 195 (2006), pp 1594-1607.

[12] L.L. Thompson, *A review of finite element methods for time-harmonic acoustics*, J. Ac. Soc. Am., Vol. 119 (2006), pp 1315-1330.

[13] B. Pluymers, B. Van Hal, D. Vandepitte, W. Desmet, *Trefftz-based methods for time-harmonic acoustics*, Arch. Comp. Meth. in Eng., Vol. 14, Iss. 4 (2007), pp 343–381.

[14] D. W. Herrin, F. Martinus, T. W. Wu, A. F. Seybert, *An assessment of the high frequency boundary element and Rayleigh integral approximations*, Applied Acoustics, Vol. 67 (2006), pp 819-833.

[15] C. Wang, J. Zhu, Q. Zhang, C. Yang, A. Parrett, M. Qian, *Simulation of vehicle exterior sound fields by high frequency boundary element method*, Proc. SAE NVH 2005 Conference, Grand Traverse, MI, USA (2005), SAE 2005-01-2328.

[16] T. Sakuma, Y. Yasuda, *Fast multipole boundary element method for large-scale steady-state sound field analysis. Part I: setup and validation*, Acustica-acta Acustica, Vol 88, No. 4 (2002), pp 513–525.

[17] M. Fischer, *The fast multipole boundary element method and its application to structure-acoustic field interaction*, PhD. thesis, Stuttgart University, Stuttgart, Germany (2004).

[18] S. Chaigne, G. Sylvand, E. Duceau, J. Simon, *On the use of the FMM for accurate automotive body panel acoustic load predictions*, Proc. SAE NVH 2007 Conference, St. Charles, IL, USA (2007), SAE 2007-01-2313.

[19] J. Cordioli, S. Müller, T. Connelly, K. Fung, *Validation of interior noise prediction obtained using Statistical Energy Analysis and Fast Multipole BEM*, Proc. SAE NVH 2009 Conference, St. Charles, IL, USA (2009), SAE 2009-01-2200.

[20] D. Berckmans, P. Kindt, P. Sas, W. Desmet, *Evaluation of substitution monopole models for tire noise sound synthesis*, Mech. Systems and Signal Proc., Vol. 24 (2010), pp 240–255.

[21] O. Von Estorff (Ed.), *Boundary elements in acoustics: advances and applications*, WIT Press, Southampton, UK (2000).

[22] Z. Zhang, N. Vlahopoulos, T. Allen, K.Y. Zhang, *Development and validation of a computational process for pass-by noise simulation*, Int. J. Vehicle Design, Vol. 34, No. 1 (2004), pp. 12–34.

[23] National Crash Analysis Center, *Dodge Neon, Detailed model*, Ashbum VA, USA(2006), retrieved from http://www.ncac.gwu.edu/vml/models.html on August 19, 2009.

[24] Virtual.Lab Acoustics, Rev. 8B-SL2, LMS International, Leuven, Belgium (2009).

[25] S. Müller, V. Cotoni, T. Connelly, *Guidelines for using fast multipole BEM to calculate automotive exterior acoustic loads in SEA models*, Proc. SAE NVH 2009 Conference, St. Charles, IL, USA (2009), SAE 2009-01-2220.

[26] D. Deschrijver, B. Gustavsen, T. Dhaene, *Fast broadband modeling of frequency-domain responses by piecewise interpolation*, El. Pow. Syst. Res., Vol 79 (2009), pp. 1574–1578.

[27] S. Marburg, *Six points per wavelength: is that enough?*, J. Comp. Acoust., Vol. 10, Iss. 1 (2002), pp. 25–51.

[28] R. D'Amico, A. Pratellesi, M. Pierini, M. Tournour, *Mitigation of the Non-Uniqueness problem for the Indirect Boundary Element Method*, Proc. Recent Advances in Structural Dynamics Conference 2010 (RASD2010), Southampton, UK (2010).

[29] P. Fiala, J. Huijssen, B. Pluymers, R. Hallez, W. Desmet, *Fast Multipole BEM modeling of head related transfer functions of a dummy head and torso*, ISMA 2010 Conference, Leuven, Belgium (2010).

[30] H. Wallén, S. Järvenpää, P. Ysä-Oijala, *Broadband multilevel fast multipole algorithm for acoustic scattering problems*, J. Comp. Acoust, Vol 14, Iss. 4 (2006), pp 507–526.

[31] N.A. Gumerov, R. Duraiswami, *A broadband fast multipole accelerated boundary element method for the three dimensional Helmholtz equation*, J. Acoust. Soc. Am, Vol. 125, Iss. 1 (2009), pp 191–205.